Available online at www.sciencedirect.com
SCIENCE DIRECT®
Journal of Computational Physics 208 (2005) 116–133
JOURNAL OF COMPUTATIONAL PHYSICS
www.elsevier.com/locate/jcp

A locking-free meshless local Petrov–Galerkin formulation for thick and thin plates

Q. Li [a,*], J. Soric [b], T. Jarak [b], S.N. Atluri [a]

[a] *Center for Aerospace Research and Education, University of California, Irvine, 5251 California Avenue, #140, Irvine, CA 92612, USA*
[b] *Department of Mechanical Engineering and Naval Architecture, University of Zagreb, 10000 Zagreb, I. Lučića 5, Croatia*

Received 19 August 2004; received in revised form 8 February 2005; accepted 9 February 2005
Available online 13 April 2005

Abstract

In this paper, a locking-free meshless local Petrov–Galerkin formulation is presented for shear flexible thick plates, which remains theoretically valid in the thin-plate limit. The kinematics of a three-dimensional solid is used, instead of the conventional plate assumption. The local symmetric weak form is derived for cylindrical shaped local sub-domains. The numerical characteristics of the local symmetric weak form, in the thin plate limit, are discussed. Based on this discussion, the shear locking is theoretically eliminated by changing the two dependent variables in the governing equations. The moving least square interpolation is utilized in the in-plane numerical discretization for all the three displacement components. In the thickness direction, on the other hand, a linear interpolation is used for in-plane displacements, while a hierarchical quadratic interpolation is utilized for the transverse displacement, in order to eliminate the thickness locking. Numerical examples in both the thin plate limit and the thick plate limit are presented, and the results are compared with available analytical solutions.

Keywords: Meshless method; Meshless local Petrov–Galerkin methods; Local symmetric weak form; Moving least squares interpolation; Solid plate; Shear locking; Thickness locking

1. Introduction

The meshless local Petrov–Galerkin (MLPG) method is a truly meshless method, which requires no elements or background cells, for either the interpolation or the integration purposes. The concept of MLPG was first proposed by Atluri and Zhu [1], and later discussed in depth in Atluri and Shen [2,3], and in Atluri

* Corresponding author. Tel.: +1 949 824 9947; fax: +1 949 824 3584.
E-mail address: qiuzhanl@uci.edu (Q. Li).

0021-9991/$ - see front matter © 2005 Elsevier Inc. All rights reserved.
doi:10.1016/j.jcp.2005.02.008

[4]. The most significant difference between this method and the finite element method or any other meshless method, is that the local weak forms are generated on overlapping local sub-domains, instead of using the global weak form. Integration of the weak form is performed in local sub-domains with simple geometrical shapes; therefore no elements or background cells are necessary either for interpolation purposes or for integration purposes. The MLPG methods have found a wide range of application in 2-D elasto-statics [5], 2-D elasto-dynamics [6], fluid mechanics [7], convection-diffusion problems [8], thin plates [9], thick plates [10], fracture mechanics [11,12], electromagnetic field computations [13], strain gradient theory [14], and multiscale simulations [15]. More recently, significant efforts have been devoted to the development of the MLPG method in the 3-D regime. Li et al. [16] applied MLPG domain discretization method to 3-D elasto-statics. Han and Atluri [17] applied the MLPG BIE methods to 3-D elastic fracture problems. A detailed comparison of the performance of the MLPG methods, in 3-D problems, was carried out by Han and Atluri [18]. A more stable and efficient numerical integration scheme to evaluate the weak-forms was also proposed in the same paper. Han and Atluri [19] also applied the MLPG domain discretization method to 3-D elasto-dynamic problems of impact and fragmentation.

Sorić et al. [20] applied the 3-D MLPG method to study thick solid plates. By using the kinematics of a 3-D continuum, the plate was described by sets of two nodes located on the upper and lower surface of the plate. The local symmetric weak forms were generated on the cylindrical local sub-domains that surround each set of nodes on the plate surfaces. The trial function in the in-plane directions was interpolated by a 2-D moving least squares (MLS) approximation. The test function was of a linear form. Promising results were obtained for thick plates, with thickness to span ratio greater than 1/20. However, the drawback of shear locking appeared in the case of thin plates, when the thickness to span ratios were less than 1/20.

In the current paper, a totally locking-free 3-D MLPG formulation is developed, which remains valid for both thick as well as thin plates. The shear locking phenomenon was previously addressed in the literature, using other meshless methods, by specially constructing the shape function of the rotation field to be the derivative of the displacement field, so that the field inconsistency could be eliminated [21,22]. In this paper, a different concept, which completely removes the locking phenomenon from its theoretical origin, is used. The concept of a locking-free weak formulation was first introduced by Atluri [23]. It was successfully applied to shear flexible beams by Cho and Atluri [24]. By properly choosing the field variables, the shear locking could be eliminated completely, a priori, without any numerical expediencies such as the reduced integration, or the use of assumed strains. Using this concept in the solid plate formulation, the generalized coordinates of the upper–lower nodes are changed to be the mid-plane displacements, and shear strain components. The corresponding locking-free local symmetric weak form is constructed over cylindrical shaped local sub-domains surrounding each upper–lower node set. No reduced-order-integration is necessary in integrating the present locking-free weak-form. A MLS approximation is used in the interpolation of field variables in the in-plane directions. Detailed numerical results, which validate the present formulation, are presented for both thick as well as thin plates.

2. MLPG formulation for a 3-D plate

The presently used concept of a 3-D plate retains the kinematics of three-dimensional continuum in the flat plate structures. The strong form governing equations are the linear momentum balance equations of a 3-D solid:

$$\sigma_{ij,j} + b_i = 0, \tag{1}$$

$$u_i = \bar{u}_i, \quad \text{on } \Gamma_u, \tag{2a}$$

$$t_i = \sigma_{ij} n_j = \bar{t}_i, \quad \text{on } \Gamma_t, \tag{2b}$$

where σ_{ij} are the components of the symmetric stress tensor, b_i are the body forces, $\bar{u}_i$ are the prescribed displacements, $\bar{t}_i$ are the prescribed surface tractions, n_j are the components of a unit outward normal to the global boundary, Γ_u is the part of global boundary with prescribed displacements, and Γ_t is the part of global boundary with prescribed surface tractions.

The plate is discretized with the set of two nodes on the upper and lower surfaces, respectively. Instead of writing the global weak form for the governing equations, the MLPG method constructs the weak forms over local sub-domains, which are taken as cylinders standing between upper and lower surfaces around each node set (Fig. 1).

The local unsymmetric weak form over the Jth local sub-domain is

$$\int_{\Omega_s^J} (\sigma_{ij,j} + b_i) v_i \, d\Omega - \alpha \int_{\Gamma_{su}^J} (u_i - \bar{u}_i) v_i \, d\Gamma = 0, \tag{3}$$

where u_i is the trial function for the displacement field, Ω_s^J is the local sub-domain surrounding the Jth node set, Γ_{su}^J is the part of the boundary of the local sub-domain with the prescribed displacements $\bar{u}_i$, and α denotes a penalty parameter.

By applying the divergence theorem, the local symmetric weak form could be derived as

$$\int_{\Gamma_s^J} \sigma_{ij} v_i n_j \, d\Gamma - \int_{\Omega_s^J} \sigma_{ij} v_{i,j} \, d\Omega + \int_{\Omega_s^J} b_i v_i \, d\Omega - \alpha \int_{\Gamma_{su}^J} (u_i - \bar{u}_i) v_i \, d\Gamma = 0. \tag{4}$$

We assume the test function v_i to be linear in the thickness direction, as

$$v_i = v_{0i} + x_3 v_{1i}, \tag{5}$$

where v_{0i} and v_{1i} are arbitrary constants.

By substituting the above test functions into Eq. (4) and imposing the boundary condition in Eq. (2b), one obtains

$$\begin{aligned} &\left(\int_{L_s^J} t_i \, d\Gamma + \int_{\Gamma_{su}^J} t_i \, d\Gamma + \int_{\Gamma_{st}^J} \bar{t}_i \, d\Gamma + \int_{\Omega_s^J} b_i \, d\Omega - \alpha \int_{\Gamma_{su}^J} (u_i - \bar{u}_i) d\Gamma \right) v_{0i} \\ &+ \left(\int_{L_s^J} t_i x_3 \, d\Gamma + \int_{\Gamma_{su}^J} t_i x_3 \, d\Gamma + \int_{\Gamma_{st}^J} \bar{t}_i x_3 \, d\Gamma + \int_{\Omega_s^J} (b_i x_3 - \sigma_{i3}) d\Omega - \alpha \int_{\Gamma_{su}^J} (u_i - \bar{u}_i) x_3 \, d\Gamma \right) v_{1i} = 0. \end{aligned} \tag{6}$$

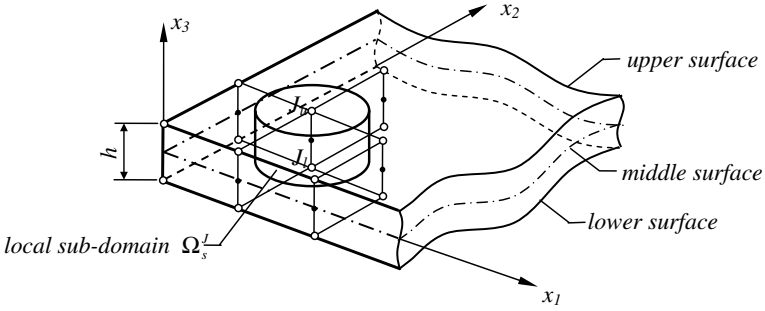

Fig. 1. Nodal location and local sub-domain.

Herein the boundary Γ_s^J of the Jth local sub-domain consists of three parts, $\Gamma_s^J = L_s^J \cup \Gamma_{st}^J \cup \Gamma_{su}^J$. L_s^J is the local boundary that is totally inside global domain. Γ_{st}^J is the part of local boundary that coincides with the global traction boundary, i.e., $\Gamma_{st}^J = \Gamma_s^J \cap \Gamma_t$. Γ_{su}^J is the part of local boundary that coincides with the global geometric boundary, i.e., $\Gamma_{su}^J = \Gamma_s^J \cap \Gamma_u$.

Because v_{0i} and v_{1i} are independent of each other, Eq. (6) can be decomposed to the following set of equations

$$\int_{L_s^J} t_i \, d\Gamma + \int_{\Gamma_{su}^J} t_i \, d\Gamma + \int_{\Gamma_{st}^J} \bar{t}_i \, d\Gamma + \int_{\Omega_s^J} b_i \, d\Omega - \alpha \int_{\Gamma_{su}^J} (u_i - \bar{u}_i) d\Gamma = 0, \tag{7a}$$

$$\int_{L_s^J} t_i x_3 \, d\Gamma + \int_{\Gamma_{su}^J} t_i x_3 \, d\Gamma + \int_{\Gamma_{st}^J} \bar{t}_i x_3 \, d\Gamma + \int_{\Omega_s^J} (b_i x_3 - \sigma_{i3}) d\Omega - \alpha \int_{\Gamma_{su}^J} (u_i - \bar{u}_i) x_3 \, d\Gamma = 0. \tag{7b}$$

Therefore, six governing equations are generated for each local sub-domain.

3. Locking-free formulation

Locking phenomena are observed in the above meshless solid plate formulation. Two types of locking phenomena are addressed in the current paper, (1) shear locking in the thin plate limit; (2) thickness locking when Poisson's ratio is non-zero.

3.1. Shear locking

In finite element analysis, shear locking in a solid shell element is well documented. Various methods such as assumed strain, and reduced integration, were used for the solid shell elements in order to eliminate the shear locking [25]. A higher order interpolation was also claimed to relieve the shear locking phenomenon [26].

In order to reveal the shear locking phenomenon in the meshless solid plate formulation, a local sub-domain which does not intersect with the global boundary, with no body forces and no external forces, is examined. With these assumptions, the integrations over Γ_{su}^J, Γ_{st}^J and Ω_s^J in Eqs. (7a) and (7b) are eliminated. The governing equations simply become

$$\int_{L_s^J} t_i \, d\Gamma = \int_{-\frac{h}{2}}^{\frac{h}{2}} \int_0^{2\pi} t_i R \, d\theta \, dx_3 = R \int_{-\frac{h}{2}}^{\frac{h}{2}} \int_0^{2\pi} n_j E_{ijkl} \frac{1}{2} \left(\frac{\partial u_k}{\partial x_l} + \frac{\partial u_l}{\partial x_k} \right) d\theta \, dx_3 = 0, \quad (i,j,k = 1,2,3), \tag{8a}$$

$$\int_{L_s^J} t_i x_3 \, d\Gamma - \int_{\Omega_s^J} \sigma_{i3} \, d\Omega = R \int_{-\frac{h}{2}}^{\frac{h}{2}} \int_0^{2\pi} n_j E_{ijkl} \frac{1}{2} \left(\frac{\partial u_k}{\partial x_l} + \frac{\partial u_l}{\partial x_k} \right) x_3 \, d\theta \, dx_3 - \int_{-\frac{h}{2}}^{\frac{h}{2}} \int_0^{2\pi} \int_0^R E_{i3kl} \frac{1}{2} \left(\frac{\partial u_k}{\partial x_l} + \frac{\partial u_l}{\partial x_k} \right) r \, dr \, d\theta \, dx_3 = 0, \quad (i,j,k = 1,2,3), \tag{8b}$$

where R is the radius of the cylindrical local sub-domain, h is the thickness of the plate, n_j is the outward normal on L_s^J, E_{ijkl} is the tensor of elastic constants. If a linear interpolation in the thickness direction is used for displacements, the plate deformation can be described as

$$\begin{cases} u_\alpha = u_{\alpha 0}(x_\beta) + x_3 u_{\alpha 1}(x_\beta), \\ u_3 = u_{30}(x_\beta) + x_3 u_{31}(x_\beta), \end{cases} \quad (\alpha, \beta = 1,2), \tag{9}$$

where $u_{\alpha 0}$ and u_{30} are the mid-surface displacements, while $u_{\alpha 1}$ and u_{31} describe the total rotations. The derivatives of the displacements become:

$$\begin{cases} \dfrac{\partial u_i}{\partial x_\alpha} = \dfrac{\partial u_{i0}}{\partial x_\alpha} + x_3 \dfrac{\partial u_{i1}}{\partial x_\alpha}, \\ \dfrac{\partial u_i}{\partial x_3} = u_{i1}. \end{cases} \tag{10}$$

Substituting Eq. (10) into Eqs. (8a) and (8b) and integrating through the thickness, we have:

$$\int_{L_s^J} t_i \, \mathrm{d}\Gamma = Rh \int_0^{2\pi} n_j \left[E_{ij\alpha\beta} \frac{1}{2} \left(\frac{\partial u_{\alpha 0}}{\partial x_\beta} + \frac{\partial u_{\beta 0}}{\partial x_\alpha} \right) + E_{ij3\alpha} \left(\frac{\partial u_{30}}{\partial x_\alpha} + u_{\alpha 1} \right) + E_{ij33} u_{31} \right] \mathrm{d}\theta = 0, \tag{11a}$$

$$\begin{aligned} \int_{L_s^J} t_i x_3 \, \mathrm{d}\Gamma - \int_{\Omega_s} \sigma_{i3} \, \mathrm{d}\Omega = {} & R \frac{h^3}{12} \int_0^{2\pi} \left\{ n_j \left[E_{ij\alpha\beta} \frac{1}{2} \left(\frac{\partial u_{\alpha 1}}{\partial x_\beta} + \frac{\partial u_{\beta 1}}{\partial x_\alpha} \right) + E_{ij3\alpha} \left(\frac{\partial u_{31}}{\partial x_\alpha} \right) \right] \right\} \mathrm{d}\theta - h \\ & \times \int_0^{2\pi} \int_0^R \left\{ \left[E_{i3\alpha\beta} \frac{1}{2} \left(\frac{\partial u_{\alpha 0}}{\partial x_\beta} + \frac{\partial u_{\beta 0}}{\partial x_\alpha} \right) + E_{i33\alpha} \left(\frac{\partial u_{30}}{\partial x_\alpha} + u_{\alpha 1} \right) + E_{i333} u_{31} \right] \right\} r \, \mathrm{d}r \, \mathrm{d}\theta \\ = {} & 0. \end{aligned} \tag{11b}$$

Consider the case when $u_{\alpha 0}$, $u_{\alpha 1}$, u_{30}, u_{31} are interpolated by a meshless interpolation. While these interpolations will not be exactly polynomials in r and θ in each domain, for a C_1 continuous trial function, one may consider their constant components and components that are approximately linear in r. Let

$$u_{\alpha 1} = D_{\alpha 0} + D_{\alpha 1} r + \text{higher order terms}. \tag{12}$$

Then it is seen that the first integrand on left hand side of Eq. (11b) will lead to a term of the type $D_{\alpha 1} R h^3$, while the second integrand on the left hand side of Eq. (11b) will lead to a term of the type $D_{\alpha 1} R^3 h$ In the thin plate limit ($h \to 0$), we have

$$\frac{R^3 h}{R h^3} = \frac{R^2}{h^2} \to \infty. \tag{13}$$

Thus, the algebraic equation corresponding to Eq. (11b) in the limit as $h \to 0$ leads to the condition $D_{\alpha 1} \to 0$. Thus, $u_{\alpha 1} \to D_{\alpha 0}$ which means "constant" total rotation or zero bending moment in Eq. (11b). However, in the thin plate limit, bending not only exists, but, it is also expected to be the dominant behavior. Hence, the exact integration will lead to an overly stiff result, and the system locks. In order to eliminate the shear locking phenomenon, we introduce a new variable γ_α, such that:

$$\gamma_\alpha = \frac{\partial u_{30}}{\partial x_\alpha} + u_{\alpha 1}. \tag{14}$$

Substituting Eq. (14) into Eq. (9), we have:

$$u_\alpha = u_{\alpha 0} + x_3 \left(\gamma_\alpha - \frac{\partial u_{30}}{\partial x_\alpha} \right), \tag{15a}$$

$$u_3 = u_{30} + x_3 u_{31}. \tag{15b}$$

The field variables $u_{\alpha 0}$, u_{30}, $u_{\alpha 1}$, u_{31} are changed to $u_{\alpha 0}$, u_{30}, γ_α, u_{31}. The governing equation (11b) becomes

$$\begin{aligned} \int_{L_s^J} t_i x_3 \, \mathrm{d}\Gamma - \int_{\Omega_s^J} \sigma_{i3} \, \mathrm{d}\Omega = {} & R \frac{h^3}{12} \int_0^{2\pi} \left\{ n_j \left[E_{ij\alpha\beta} \frac{1}{2} \left(\frac{\partial \gamma_\alpha}{\partial x_\beta} + \frac{\partial \gamma_\beta}{\partial x_\alpha} - 2 \frac{\partial^2 u_{30}}{\partial x_\alpha \, \partial x_\beta} \right) + E_{ij3\alpha} \left(\frac{\partial u_{31}}{\partial x_\alpha} \right) \right] \right\} \mathrm{d}\theta - h \\ & \times \int_0^{2\pi} \int_0^R \left\{ \left[E_{i3\alpha\beta} \frac{1}{2} \left(\frac{\partial u_{\alpha 0}}{\partial x_\beta} + \frac{\partial u_{\beta 0}}{\partial x_\alpha} \right) + E_{i33\alpha} \gamma_\alpha + E_{i333} u_{31} \right] \right\} r \, \mathrm{d}r \, \mathrm{d}\theta \\ = {} & 0. \end{aligned} \tag{16}$$

Let γ_α be approximated as

$$\gamma_\alpha = C_{\alpha 0} + C_{\alpha 1} r + \text{higher order term.} \tag{17}$$

The first integrand will contain a term of the type $C_{\alpha 1} R h^3$. The second integrand will contain a term of the type $C_{\alpha 1} R^3 h$. In the thin plate limit, the algebraic equation corresponding to Eq. (16) will lead to the conditions $C_{\alpha 1} \to 0$ and $C_{\alpha 0} \to 0$. Thus, $\gamma_\alpha \to 0$; this is physically correct, and does not lead to locking in the bending behavior in the plate.

3.2. Thickness locking

It is well known that if the Poisson's ratio is non-zero, when bending occurs in the plate, the strain in the out-of-plane direction ε_{33} varies linearly in the thickness direction, due to the coupling between the linear in-plane strains and the normal stress in the thickness direction. Therefore, the linear assumption of $u_3 = u_{30} + x_3 u_{31}$ in Eq. (15b) will lead to an inaccurate result, which is the well known "thickness-locking" phenomenon. Hauptmann et al. [25] introduced another degree of freedom, at the midpoint in a solid shell element, in order to introduce a quadratic interpolation in the thickness direction. A similar technique is used in the current paper. The out-of-plane displacement u_3 is assumed to be in the form of

$$u_3 = u_{30} + x_3 u_{31} + \xi u_{32}, \tag{18}$$

where

$$\xi = \frac{1}{2}\left(1 - \frac{x_3^2}{\left(\frac{h}{2}\right)^2}\right).$$

Hence, for each local sub-domain, we have seven unknowns: $u_{\alpha 0}$, u_{30}, γ_α, u_{31}, and u_{32}.

Because we have only six governing equations from the local symmetric weak form, an additional governing equation needs to be constructed. In order to obtain the 7th equation, the equilibrium is enforced at the midpoint for each local sub-domain, and the collocation method with the Dirac's Delta function $\delta(\mathbf{x} - \bar{\mathbf{x}}_J)$ as the test function, is used. The additional governing equation in the out-of-plane direction becomes

$$\sigma_{3j,j}(\bar{\mathbf{x}}_J) + b_3(\bar{\mathbf{x}}_J) = 0, \tag{19}$$

where $\bar{\mathbf{x}}_J$ is the location of the midpoint for the Jth local sub-domain.

4. Moving least squares approximation

In the MLPG method, the test and trial functions are not necessarily from the same function spaces. In the current formulation, the test function is chosen to be linear as in Eq. (5). The trial function in the out-of-plane direction is chosen to be as in Eqs. (15b) and (18). The trial functions for $u_{\alpha 0}$, u_{30}, γ_α, u_{31}, and u_{32}, in the in-plane directions, on the other hand, are chosen to be the two dimensional MLS interpolations over a number of nodes within the domain of influence. While the local sub-domain is defined as the support of the test function on which the integration is carried out, the domain of influence is defined as a region, where the weight functions of the nodes inside do not vanish in the local sub-domain of the current node (Fig. 2). In other words, the domain of influence contains all the nodes that have non-zero coupling with the current nodal values in the stiffness matrix.

The characteristics of MLS have been widely discussed in literatures [27,28]. The MLS approximation of any function u for any point $\mathbf{x} \in \Omega_s^J$, is defined by

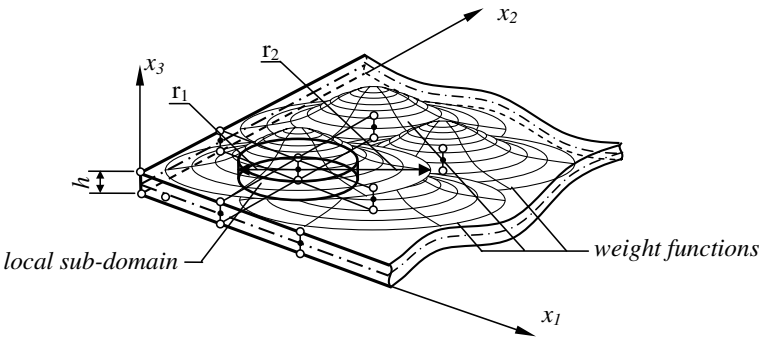

Fig. 2. Local sub-domains and weight functions.

$$u^h = \mathbf{p}^{\mathrm{T}}(\mathbf{x})\mathbf{a}(\mathbf{x}), \quad \mathbf{x} \in \Omega_{\mathrm{s}}^J, \tag{20}$$

where $\mathbf{p}^{\mathrm{T}}(\mathbf{x}) = [p_1(\mathbf{x}),p_2(x),\ldots,p_m(\mathbf{x})]$ is a complete monomial basis of order m. It needs to be mentioned here that only the in-plane displacement components are considered in the above vector $\mathbf{x}$, i.e., $\mathbf{x} = [x_1,x_2]$, because MLS is only used as in-plane interpolation of the field vectors.

Quadratic basis is used in the current paper

$$\mathbf{p}^{\mathrm{T}}(\mathbf{x}) = \left[1, x_1, x_2, x_1^2, x_2^2, x_1x_2\right], \tag{21}$$

$\mathbf{a}(\mathbf{x})$ is a coefficient vector which is defined by minimizing a weighted discrete L_2-norm

$$J(\mathbf{a}(\mathbf{x})) = \sum_{I=1}^{N} w_I(\mathbf{x})\left[\mathbf{p}(\mathbf{x}_I)\mathbf{a}(\mathbf{x}) - \hat{u}^I\right]^2 = [\mathbf{P}\cdot\mathbf{a}(\mathbf{x}) - \hat{\mathbf{u}}]^{\mathrm{T}}\cdot\mathbf{W}(\mathbf{x})\cdot[\mathbf{P}\cdot\mathbf{a}(\mathbf{x}) - \hat{\mathbf{u}}], \tag{22}$$

where $\mathbf{x}_I$ is the position of the Ith node whose weight function w_I does not vanish at $\mathbf{x}$.

$$\mathbf{P} = \begin{bmatrix} \mathbf{p}^{\mathrm{T}}(\mathbf{x}_1) \\ \mathbf{p}^{\mathrm{T}}(\mathbf{x}_2) \\ \cdots \\ \mathbf{p}^{\mathrm{T}}(\mathbf{x}_N) \end{bmatrix}_{N\times m}, \quad \mathbf{W} = \begin{bmatrix} w_1(\mathbf{x}) & \cdots & 0 \\ \vdots & \ddots & \vdots \\ 0 & \cdots & w_N(\mathbf{x}) \end{bmatrix}_{N\times N}, \quad \hat{\mathbf{u}} = \left[\hat{u}^1, \hat{u}^2, \ldots, \hat{u}^N\right]_{1\times N},$$

where $\hat{u}^I$, $I = 1, 2,\ldots, N$ are the fictitious nodal values. It needs to be mentioned that in MLS interpolation, the fictitious nodal value $\hat{u}^I$ does not equal to the approximated value u^h. The stationary condition of $J(\mathbf{x})$ with respect to the coefficients $\mathbf{a}(\mathbf{x})$ leads to the following linear relation

$$\mathbf{A}(\mathbf{x})_{m\times m}\mathbf{a}(\mathbf{x})_{m\times 1} = \mathbf{B}(\mathbf{x})_{m\times N}\hat{\mathbf{u}}_{N\times 1}, \tag{23}$$

where

$$\mathbf{A}(\mathbf{x}) = \mathbf{P}^{\mathrm{T}}\mathbf{W}\mathbf{P} = \sum_{I=1}^{N} w_I\mathbf{p}(\mathbf{x}_I)\mathbf{p}^{\mathrm{T}}(\mathbf{x}_I), \tag{24}$$

$$\mathbf{B}(\mathbf{x}) = \mathbf{P}^{\mathrm{T}}\mathbf{W} = [w_1(\mathbf{x})\mathbf{p}(\mathbf{x}_1), w_2(\mathbf{x})\mathbf{p}(\mathbf{x}_2), \ldots, w_N(\mathbf{x})\mathbf{p}(\mathbf{x}_N)]. \tag{25}$$

By substituting $\mathbf{a}(\mathbf{x})$ into Eq. (20), the interpolation function $u^h(\hat{u}^I)$ is obtained

$$u^h = \sum_{I=1}^{N} \phi^I(\mathbf{x})\hat{u}^I, \tag{26}$$

where $\phi^I(\mathbf{x}) = \sum_{j=1}^{m} p_j(\mathbf{x})[\mathbf{A}^{-1}(\mathbf{x})\mathbf{B}(\mathbf{x})]_{jI}$.

Due to the higher-order nature of the plate problem, a 5th order spline type weight function is used:

$$w_I(\mathbf{x}) = \begin{cases} 1 - 10\left(\frac{d_I}{r_I}\right)^3 + 15\left(\frac{d_I}{r_I}\right)^4 - 6\left(\frac{d_I}{r_I}\right)^5 & 0 \leqslant d_I \leqslant r_I, \\ 0 & d_I \leqslant r_I. \end{cases} \tag{27}$$

Thus, a C_2 continuity, in the in-plane coordinates, is guaranteed for the trial function.

5. Numerical discretization

The in-plane MLS interpolations for $u_{\alpha 0}$, u_{30}, γ_α, u_{31}, and u_{32}, leads to:

$$u^h_{\alpha 0} = \sum_{I=1}^{N} \phi^I \hat{u}^I_{\alpha 0}, \tag{28a}$$

$$u^h_{30} = \sum_{I=1}^{N} \phi^I \hat{u}^I_{30}, \tag{28b}$$

$$\gamma^h_\alpha = \sum_{I=1}^{N} \phi^I \hat{\gamma}^I_\alpha, \tag{28c}$$

$$u^h_{31} = \sum_{I=1}^{N} \phi^I \hat{u}^I_{31}, \tag{28d}$$

$$u^h_{32} = \sum_{I=1}^{N} \phi^I \hat{u}^I_{32}. \tag{28e}$$

Substituting Eqs. (28a)–(28e) to Eqs. (15a) and (18), the displacements are discretized to

$$\begin{Bmatrix} u_1 \\ u_2 \\ u_3 \end{Bmatrix} = \sum_{I=1}^{N} \begin{bmatrix} \phi^I & 0 & -\phi^I_{,1}x_3 & \phi^I x_3 & 0 & 0 & 0 \\ 0 & \phi^I & -\phi^I_{,2}x_3 & 0 & \phi^I x_3 & 0 & 0 \\ 0 & 0 & \phi^I & 0 & 0 & \phi^I x_3 & \phi^I \xi \end{bmatrix} \begin{Bmatrix} \hat{u}^I_{10} \\ \hat{u}^I_{20} \\ \hat{u}^I_{30} \\ \hat{\gamma}^I_1 \\ \hat{\gamma}^I_2 \\ \hat{u}^I_{31} \\ \hat{u}^I_{32} \end{Bmatrix} = \sum_{I=1}^{N} \mathbf{\Phi}^I \hat{\mathbf{u}}^I, \tag{29}$$

where $\phi^I(x_1,x_2)$ is the shape function of the MLS approximation for the Ith node, $\hat{u}^I_{\alpha 0}$, $\hat{u}^I_{30}$, $\hat{\gamma}^I_\alpha$, $\hat{u}^I_{31}$, $\hat{u}^I_{32}$ are the fictitious nodal values, and N is the total number of node sets in the domain of influence. Stresses can be calculated by taking the derivatives of Eq. (29) and by multiplying with the constitutive matrix. Surface

tractions can then be calculated from the stresses. Therefore, the discretized governing equations for the Jth local sub-domain have the final form of

$$\begin{aligned}
&\sum_{I=1}^{N}\left[\int_{L_s^J}\mathbf{NDB}^I\,\mathrm{d}\Gamma+\int_{\Gamma_{su}^J}\mathbf{NDB}^I\,\mathrm{d}\Gamma-\alpha\int_{\Gamma_{su}^J}\mathbf{\Phi}^I\,\mathrm{d}\Gamma\right]\hat{\mathbf{u}}^I=-\int_{\Gamma_{st}^J}\bar{\mathbf{t}}\,\mathrm{d}\Gamma-\int_{\Omega_s^J}\mathbf{b}\,\mathrm{d}\Omega-\alpha\int_{\Gamma_{su}^J}\bar{\mathbf{u}}\,\mathrm{d}\Gamma,\\
&\sum_{I=1}^{N}\left[\int_{L_s^J}\mathbf{NDB}^I x_3\,\mathrm{d}\Gamma+\int_{\Gamma_{su}^J}\mathbf{NDB}^I x_3\,\mathrm{d}\Gamma-\int_{\Omega_s^J}\mathbf{D}'\mathbf{B}^I\,\mathrm{d}\Omega-\alpha\int_{\Gamma_{su}^J}\mathbf{\Phi}^I x_3\,\mathrm{d}\Gamma\right]\hat{\mathbf{u}}^I\\
&\quad=-\int_{\Gamma_{st}^J}\bar{\mathbf{t}}x_3\,\mathrm{d}\Gamma-\int_{\Omega_s^J}\mathbf{b}x_3\,\mathrm{d}\Omega-\alpha\int_{\Gamma_{su}^J}\bar{\mathbf{u}}x_3\,\mathrm{d}\Gamma',\\
&\sum_{I=1}^{N}\mathbf{S}^I\hat{\mathbf{u}}^I=-b_3(\bar{\mathbf{x}}),
\end{aligned}\tag{30}$$

where $b_3(\bar{\mathbf{x}})$ is the 3rd component of body force at mid-plane,

$$\mathbf{N}=\begin{bmatrix}n_1&0&0&n_2&0&n_3\\0&n_2&0&n_1&n_3&0\\0&0&n_3&0&n_2&n_1\end{bmatrix},\quad \mathbf{\Phi}^I=\begin{bmatrix}\phi^I&0&0\\0&\phi^I&0\\0&0&\phi^I\end{bmatrix},$$

$$\mathbf{B}^I=\begin{bmatrix}\phi^I_{,1}&0&-\phi^I_{,11}x_3&\phi^I_{,1}x_3&0&0&0\\0&\phi^I_{,2}&-\phi^I_{,22}x_3&0&\phi^I_{,2}x_3&0&0\\0&0&0&0&0&\phi^I&-4\frac{x_3}{h^2}\phi^I\\\phi^I_{,2}&\phi^I_{,1}&-2\phi^I_{,12}x_3&\phi^I_{,2}x_3&\phi^I_{,1}x_3&0&0\\0&0&0&0&\phi_i&\phi^I_{,2}x_3&\phi^I_{,2}\xi\\0&0&0&\phi^I&0&\phi^I_{,1}x_3&\phi^I_{,1}\xi\end{bmatrix},$$

$$\mathbf{D}=D_0\begin{bmatrix}1&\frac{v}{1-v}&\frac{v}{1-v}&0&0&0\\\frac{v}{1-v}&1&\frac{v}{1-v}&0&0&0\\\frac{v}{1-v}&\frac{v}{1-v}&1&0&0&0\\0&0&0&\frac{1-2v}{2(1-v)}&0&0\\0&0&0&0&\frac{1-2v}{2(1-v)}&0\\0&0&0&0&0&\frac{1-2v}{2(1-v)}\end{bmatrix},\quad \text{where } D_0=\frac{E(1-v)}{(1+v)(1-2v)},$$

$$\mathbf{D}'=\begin{bmatrix}D_{61}&D_{62}&D_{63}&D_{64}&D_{65}&D_{66}\\D_{51}&D_{52}&D_{53}&D_{54}&D_{55}&D_{56}\\D_{31}&D_{32}&D_{33}&D_{34}&D_{35}&D_{36}\end{bmatrix},$$

$$\mathbf{S}^I=\begin{bmatrix}0&0&-D_{31}\phi^I_{,11}-D_{32}\phi^I_{,22}&(D_{31}+D_{66})\phi^I_{,1}&(D_{32}+D_{55})\phi^I_{,2}&\left(D_{55}\phi^I_{,22}+D_{66}\phi^I_{,11}\right)x_3&-\frac{4}{h^2}D_{33}\phi^I+\xi\left(D_{55}\phi^I_{,22}+D_{66}\phi^I_{,11}\right)\end{bmatrix}.$$

For each local sub-domain, seven equations in the form of Eq. (30) are generated, in terms of the seven fictitious unknowns. The actual upper–lower nodal displacements are obtained from the solved fictitious values using Eq. (29).

6. Numerical example

Three numerical experiments have been performed, in order to illustrate the effectiveness of the present method. Standard patch tests of a plate under uniform membrane tension, and under uniform pressure, are first carried out. Cantilever beams in both the thin beam limit, as well as the thick beam limit, are simulated and the results are compared with the analytical solutions. Square plates under distributed load, in both the thin and the thick plate limits are also analyzed, and the results are compared with the analytical solutions.

6.1. Plate under uniform tension

A plate under the in-plane uniform tension is considered, in order to check the membrane responses of the plate (Fig. 3). A plate under uniform pressure is also analyzed in order to check its compression response (Fig. 4). The material parameters are taken as $E = 1.0$, and $v = 0.3$. The plate is modeled with 18 nodes, including 9 nodes on the top surface and 9 nodes on the bottom surface. In the membrane test, uniform tension is applied on the right end of the plate and proper displacement constraints are applied to the left end. In the compression test, the uniform pressure is applied on the top surface of the plate, and proper displacement constrains are applied to bottom surface. The satisfaction of the first patch test requires that the displacements are linear on the lateral surfaces, and are constant on the loaded surface; and the normal stresses are constant on all the surfaces at the second patch test. Cylindrical local sub-domains with the radius of $0.8l$ are used in the analysis, where l is the nodal distance in the in-plane direction. Three-point Gauss quadrature is used for the numerical integration in cylindrical local coordinates. The present method passes both of the patch tests.

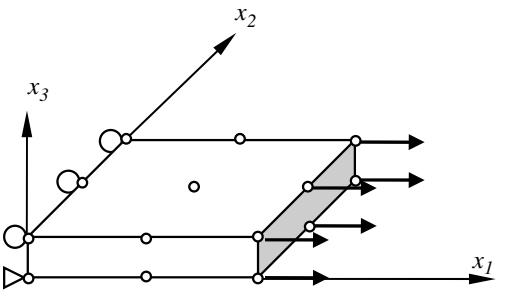

Fig. 3. Patch test: plate under uniform membrane tension.

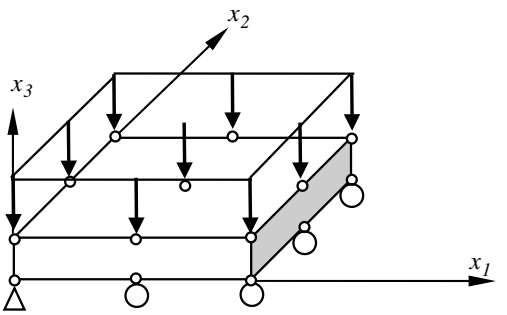

Fig. 4. Patch test: plate under uniform pressure.

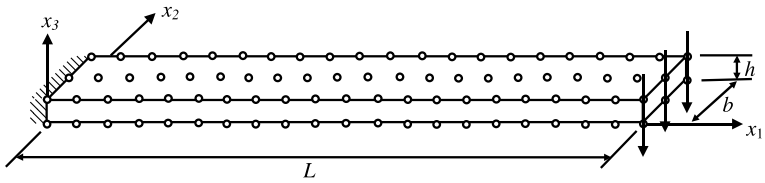

Fig. 5. Cantilever beams under a transverse load.

6.2. Cantilever beam in thick and thin beam limit

Cantilever beams under a transverse load are analyzed. A fixed length of $L = 10$ and a unit width $b = 1$ are used. The material properties are $E = 1{,}000{,}000$ and $v = 0.25$. In the in-plane direction, a uniform nodal distribution with a distance of 0.5 is used for all the cases (Fig. 5). A total of $21 \times 3 \times 2$ nodes are used in the analysis.

The theoretical solution was given in Timoshenko and Goodier [30]:

$$\begin{aligned} u_x &= -\frac{P(1-\bar{v}^2)}{6b\bar{E}I}\left(y-\frac{h}{2}\right)\left[3x(2L-x)+\frac{2-\bar{v}}{1-\bar{v}}y(y-h)\right], \\ u_y &= \frac{P(1-\bar{v}^2)}{6b\bar{E}I}\left[x^2(3L-x)+\frac{3\bar{v}}{1-\bar{v}}(L-x)\left(y-\frac{h}{2}\right)^2+\frac{4+\bar{v}}{4-4\bar{v}}h^2x\right], \end{aligned} \tag{31}$$

where I is the area moment of inertia of the beam, as

$$I = \frac{h^3}{12} \tag{32}$$

and

$$\bar{E} = \begin{cases} E \\ \frac{1+2v}{(1+v)^2}E \end{cases} \quad \text{and} \quad \bar{v} = \begin{cases} \bar{v} & \text{for plane strain,} \\ \frac{v}{1+v} & \text{for plane stress.} \end{cases} \tag{33}$$

A total of five cases with the beam thickness h equals to 2, 1, 0.1, 0.01, 0.001 are analyzed. The slenderness ratio of L/h of the five cases are 5, 10, 100, 1000 and 10,000, respectively.

The transverse deformation of the thick beam with $h = 2$ are shown in Fig. 6. The transverse deformation of the thin beam with $h = 0.001$ are shown in Fig. 7. Four different weight function support sizes are used in both the thick beam and thin beam analysis. The best solutions are obtained when the ratio R of the local sub-domain radius (r_1), to the weight function support radius (r_2), i.e., $R = r_1/r_2$, equals to 3.5. The weight function support radius r_1, and local sub-domain radius r_2 are illustrated in Fig. 2. Using the optimum support size, the tip displacements normalized with the exact solution for all the five cases are plotted in Fig. 8. It can be seen that in the thin beam limit, the shear locking is completely eliminated.

6.3. Square plates under distributed load

The performance of the current formulation is also evaluated by analyzing square plates under uniformly distributed loads. Two sets of boundary conditions are used: (1) the plates are simply supported on the all four sides (SSSS); (2) the plates are clamped on all four sides (CCCC). The schematic of the plates is shown in Fig. 9. Because of the symmetry of the problem, only a quarter of the plate is modeled. Isotropic material properties of $E = 1.092 \times 10^6$, $v = 0.3$ are used for all the cases. A fixed length of the square plate $a = 10$ is used.

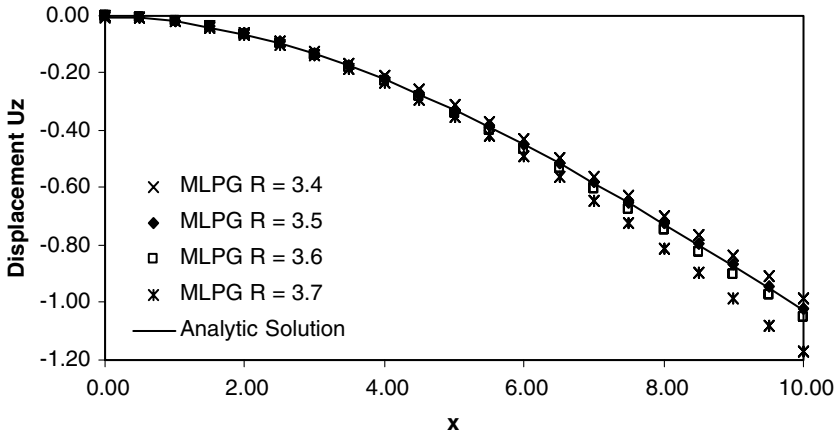

Fig. 6. Transverse deformation of thick beam ($L/h = 5$).

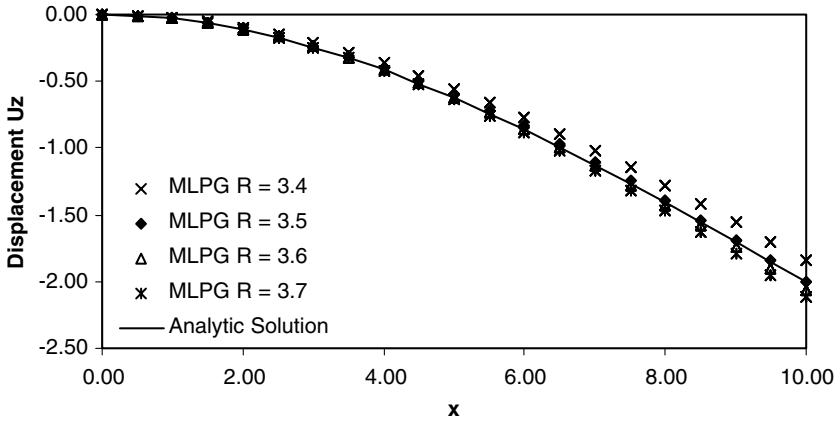

Fig. 7. Transverse deformation of thin beam ($L/h = 10{,}000$).

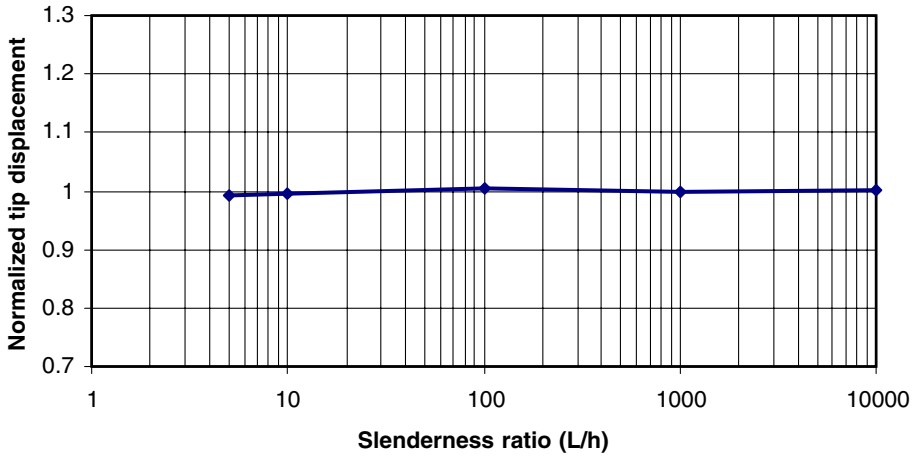

Fig. 8. Tip displacements vs. slenderness ratio.

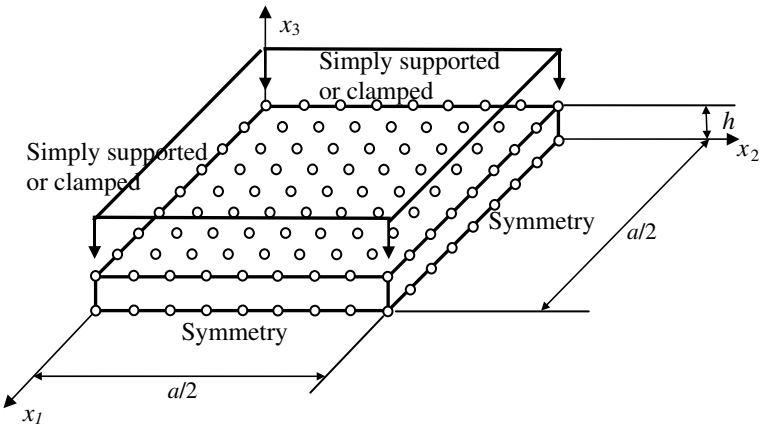

Fig. 9. Square plates under uniformly distributed load.

6.3.1. Thick plates

In the thick plate limit, four plates with different thicknesses are analyzed. Normalized theoretical center deflections were given by Srinivas and Rao [29] in Table 1. The center deflections were normalized as $\bar{W} = \frac{GW_{\max}}{hq}$, where G is the shear modulus, q is the distributed load. A parametric study is first carried out on the effects of weight function support sizes on the plate displacements. The center deflections are plotted against the varying ratios R, of the support radius to the local sub-domain radius, in Figs. 10

Table 1
Thick plates theoretical solutions

	Thickness (h)	Aspect ratio (a/h)	Normalized center deflection $Gw_{\max}/hq$ (SSSS)	Normalized center deflection $Gw_{\max}/hq$ (CCCC)
1	2.0	5.00	14.214	5.604
2	1.4	7.14	53.422	18.64
3	1.0	10.00	192.69	62.83
4	0.5	20.00	2878.2	890.3

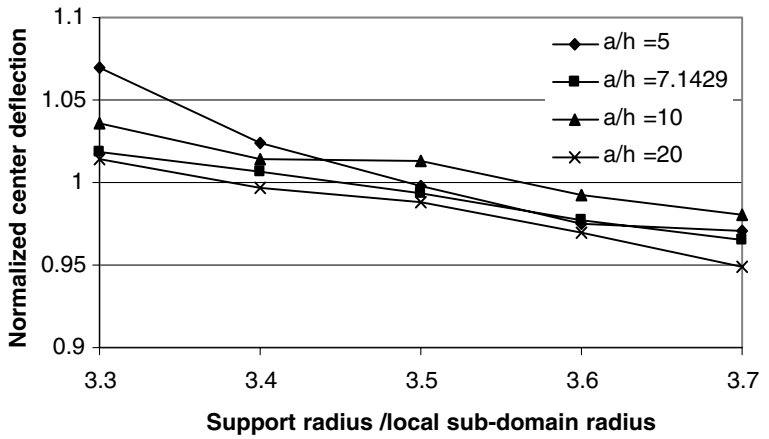

Fig. 10. Normalized center deflections vs. support sizes (CCCC).

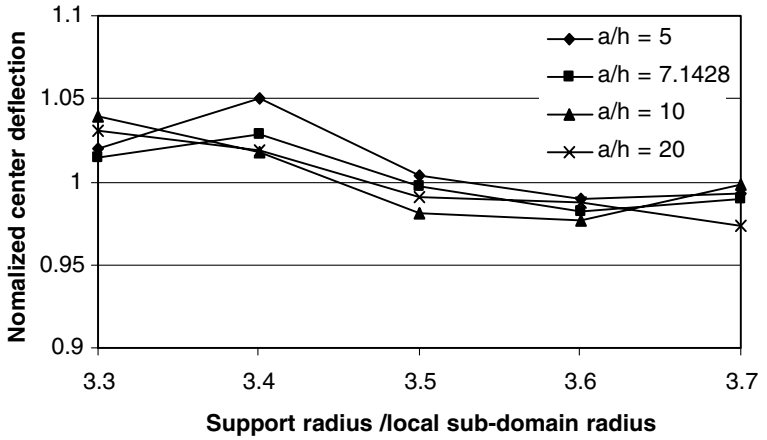

Fig. 11. Normalized center deflections vs. support sizes (SSSS).

and 11. A uniform nodal distribution of $9 \times 9 \times 2$ nodes is used in the parametric study. When changing the support size, the results oscillate around the theoretical solution and the error is within 5%. In order to study the convergence property of the current method, five additional models of $7 \times 7 \times 2$ nodes, $11 \times 11 \times 2$ nodes, $13 \times 13 \times 2$ nodes, $15 \times 15 \times 2$ nodes and $17 \times 17 \times 2$ nodes are analyzed. The convergence of center displacement for the $h = 1.0$ plate is plotted in Fig. 12.

6.3.2. Thin plates

In the thin plate limit, five cases with aspect ratio *a*/*h* equals to 100, 200, 1000, 2000 and 10,000 are analyzed. For simply supported square plates under uniformly distributed load, the theoretical maximum deflection at the center is given by Timoshenko [31]:

$$w_{\max} = \frac{4qa^4}{\pi^6 D}, \tag{34}$$

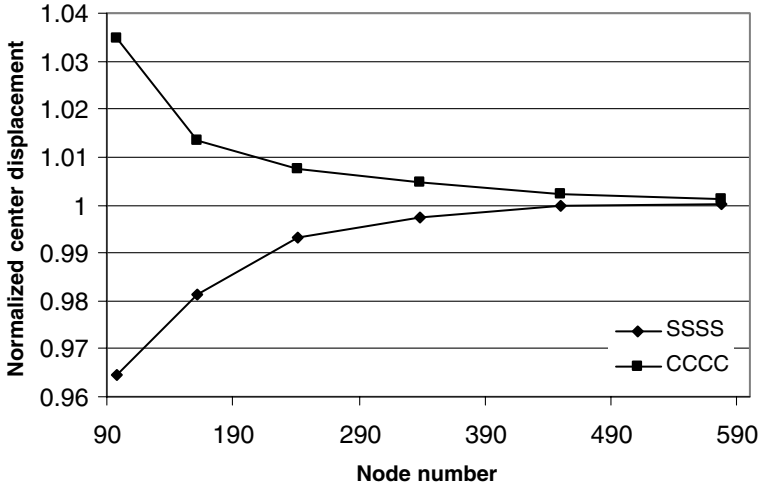

Fig. 12. Displacement convergence in thick plate limit (*a*/*h* = 10).

where D is the flexural rigidity of a plate, as

$$D = \frac{Eh^3}{12(1-\nu^2)}.$$

For clamped square plates under uniformly distributed load with $\nu = 0.3$, the maximum deflection at the center is given by Timoshenko [29]:

$$w_{\max} = 0.0138\frac{qa^4}{Eh^3}. \tag{35}$$

The effects of weight function support sizes on the plate displacements are plotted in Figs. 13 and 14. The oscillation with respect to support size is a little higher than for the thick plate, but still within a reasonable range. Five additional models with $7\times7\times2$ nodes, $11\times11\times2$ nodes, $13\times13\times2$ nodes, $15\times15\times2$ nodes and $17\times17\times2$ nodes are analyzed in the convergence study. The convergence of the center displacement for $h = 0.01$ plate is plotted in Fig. 15. The normalized central deflections are plotted for both thin plates

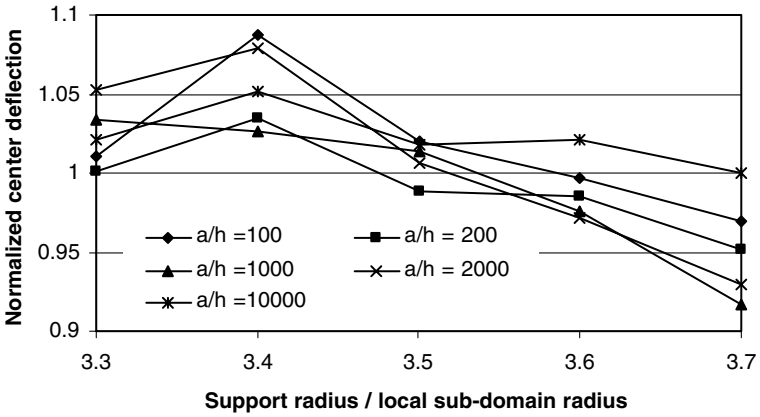

Fig. 13. Normalized center deflections vs. support sizes for thin plates (CCCC).

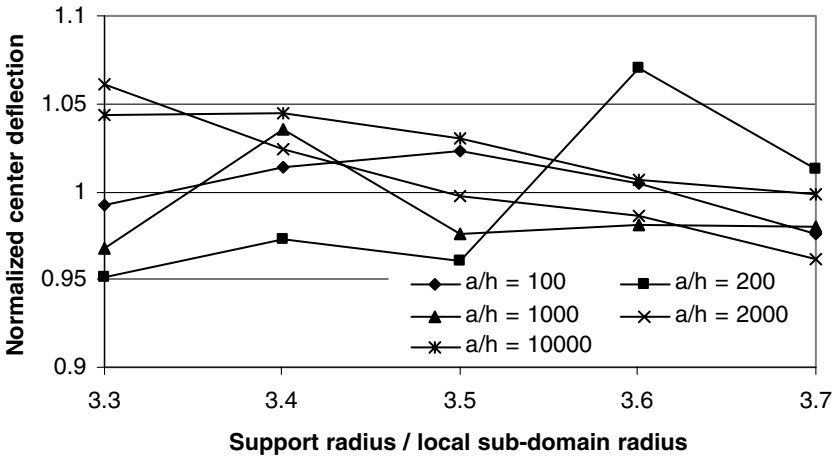

Fig. 14. Normalized center deflections vs. support sizes for thin plates (SSSS).

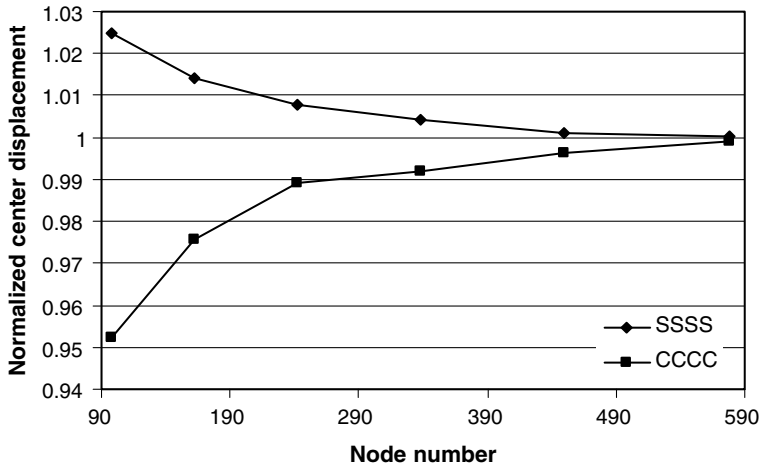

Fig. 15. Displacement convergence in thin plate limit ($a/h = 1000$).

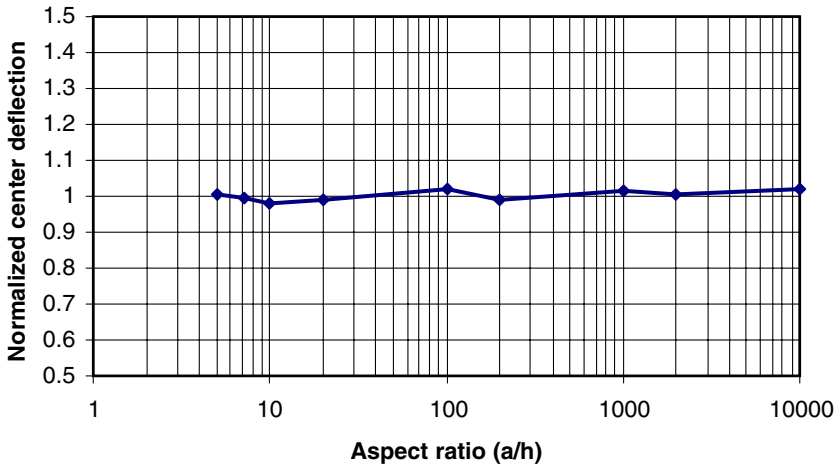

Fig. 16. Central deflections vs. aspect ratios (SSSS).

and thick plates (Fig. 16). It can be seen that shear locking is completely removed in the current formulation.

7. Conclusion

A totally locking-free MLPG formulation for plate analysis, employing a three-dimensional solid concept, is presented in this paper. Compared with the traditional five-degree-of-freedom Reissner–Mindlin plate formulation, the current formulation has seven degrees of freedom for each node set. The solid plate concept is prone to shear locking and thickness locking phenomena. Instead of using numerical techniques such as assumed strain and reduced integration to eliminate shear locking, a more theoretically straightforward approach is used in the current paper. By changing two of the dependent variables, the shear locking

is completely eliminated. In order to eliminate thickness locking, the 7th degree of freedom is introduced and, thus, a quadratic out-of-plane interpolation is used for u_3.

The above methodology is applied to a cantilever beam in both the thick beam, as well as the thin beam limits. For both thick beams and thin beams, the current method matches the theoretical solution accurately. The current method is also applied to square plates under uniformly distributed load. Both simply supported and clamped boundary conditions are used in the analysis. In both the thick plate as well as the thin plate limits, the present MLPG results agree with the analytical solution accurately.

The current solid plate formulation provides another useful member in the MLPG tool box. It is accurate, theoretically straightforward and most importantly, locking-free. It may also be extended, in a straightforward manner to shells.

Acknowledgements

This work was supported by ARL and ONR. The Authors thanks Dr. Raju Namburu, and Y.D.S. Rajapakse for helpful comments.

References

[1] S.N. Atluri, T. Zhu, A new meshless local Petrov–Galerkin (MLPG) approach in computational mechanics, Comput. Mech. 22 (1998) 117–127.
[2] S.N. Atluri, S. Shen, The meshless local Petrov–Galerkin (MLPG) method: a simple and less-costly alternative to the finite element and boundary element methods, CMES: Comp. Modeling Eng Sci 3 (1) (2002) 11–51.
[3] S.N. Atluri, S. Shen, The Meshless Local Petrov–Galerkin (MLPG) Method, Tech Science Press, 2002, 480 pp.
[4] S.N. Atluri, The Meshless Method (MLPG) for Domain and BIE Discretizations, Tech Science Press, 2004, 688 pp.
[5] S.N. Atluri, T. Zhu, The meshless local Petrov–Galerkin (MLPG) approach for solving problems in elasto-statics, Comput. Mech. 25 (2000) 169–179.
[6] R.C. Batra, H.K. Ching, Analysis of elastodynamic deformation near a crack/notch tip by the meshless local Petrov–Galerkin (MLPG) Method, CMES: Comp. Modeling Eng. Sci. 3 (6) (2002) 717–730.
[7] H. Lin, S.N. Atluri, The meshless local Petrov–Galerkin (MLPG) method for solving incompressible Navier–Stokes equations, CMES: Comp. Modeling Eng. Sci. 2 (2) (2001) 117–142.
[8] H. Lin, S.N. Atluri, Meshless local Petrov–Galerkin (MLPG) method for convection-diffusion problems, CMES: Comp. Modeling Eng. Sci. 1 (2) (2000) 45–60.
[9] S. Long, S.N. Atluri, A meshless local Petrov–Galerkin (MLPG) method for solving the bending problem of a thin plate, CMES: Comp. Modeling Eng. Sci. 3 (1) (2002) 53–64.
[10] L.F. Qian, R.C. Batra, L.M. Chen, Elastostatic deformation of a thick plate by using a higher-order shear and normal deformable plate theory and two meshless local Petrov–Galerkin (MLPG) methods, CMES: Comp. Modeling Eng. Sci. 4 (1) (2003) 161–175.
[11] H.G. Kim, S.N. Atluri, Arbitrary placement of secondary nodes, and error control, in the meshless local Petrov–Galerkin (MLPG) method, CMES: Comp. Modeling Eng. Sci. 1 (3) (2000) 11–32.
[12] H.K. Ching, R.C. Batra, Determination of crack tip fields in linear elastostatics by the meshless local Petrov–Galerkin (MLPG) method, CMES: Comp. Modeling Eng. Sci. 2 (2) (2001) 273–290.
[13] G.Z. Ni, S.L. Ho, S.Y. Yang, P.H. Ni, Meshless local Petrov–Galerkin method and its application to electromagnetic field computations, Int. J. Appl. Electromagn. Mech. 19 (1–4) (2004) 111–117.
[14] Z. Tang, S. Shen, S.N. Atluri, Analysis of materials with strain-gradient effects: A meshless local Petrov–Galerkin (MLPG) approach, with nodal displacements only, CMES: Comp. Modeling Eng. Sci. 4 (1) (2003) 177–196.
[15] S. Shen, S.N. Atluri, Multiscale simulation based on the meshless local Petrov–Galerkin (MLPG) method, CMES: Comp. Modeling Eng. Sci. 5 (3) (2004) 235–256.
[16] Q. Li, S. Shen, Z.D. Han, S.N. Atluri, Application of meshless local Petrov–Galerkin (MLPG) to problems with singularities, and material discontinuities, in 3-D Elasticity, CMES: Comp. Modeling Eng. Sci. 4 (5) (2003) 571–585.
[17] Z.D. Han, S.N. Atluri, Truly meshless local Petrov–Galerkin (MLPG) solutions of traction and displacement BIEs, CMES: Comp. Modeling Eng. Sci. 4 (6) (2003) 665–678.

[18] Z.D. Han, S.N. Atluri, Meshless local Petrov–Galerkin (MLPG) approaches for solving 3D problems in elasto-statics, CMES: Comp. Modeling Eng. Sci. 6 (2) (2004) 169–188.
[19] Z.D. Han, S.N. Atluri, A meshless local Petrov–Galerkin (MLPG) approach for 3-dimensional elasto-dynamics, CMC: Comp. Mater. Continua 1 (2) (2004) 129–140.
[20] J. Sorić, Q. Li, T. Jarak, S.N. Atluri, Meshless local Petrov–Galerkin (MLPG) formulation for analysis of thick plates, CMES: Comp. Modeling Eng. Sci. 6 (4) (2004) 349–358.
[21] B.M. Donning, W.K. Liu, Meshless methods for shear-deformable beams and plates, Comput. Meth. Appl. Engrg. 152 (1998) 47–71.
[22] W. Kanok-Nukulchai, W. Barry, K. Saran-Yasoontorn, P.H. Bouillard, On elimination of shear locking in the element-free Galerkin method, Int. J. Numer. Meth. Eng. 52 (2001) 705–725.
[23] S.N. Atluri, Methods of computational mechanics, unpublished book, 1992, 1400 pp.
[24] J.Y. Cho, S.N. Atluri, Analysis of shear flexible beams, using the meshless local Petrov–Galerkin method, based on a locking-free formulation, Eng. Computations 18 (1/2) (2001) 215–240.
[25] R. Hauptmann, K. Schweizerhof, S. Doll, Extension of the 'solid-shell' concept to large elastic and large elastoplastic deformations, Int. J. Numer. Meth. Eng. 49 (2000) 1121–1141.
[26] H. Hakula, Y. Leino, J. Pitkäranta, Scale resolution, locking, and high-order finite element modelling of shells, Comp. Meth. Appl. Mech. Eng. 133 (3–4) (1996) 157–182.
[27] S.N. Atluri, H.G. Kim, J.Y. Cho, A critical assessment of the truly meshless local Petrov–Galerkin (MLPG) and local boundary integral equation (LBIE) methods, Comput. Mech. 24 (1999) 348–372.
[28] P. Breikopf, A. Rassineux, G. Touzot, P. Villon, Explicit form and efficient computation of MLS shape functions and their derivatives, Int. J. Numer. Meth. Engrg. 48 (2000) 451–466.
[29] S. Srinivas, A.K. Rao, Flexure of thick rectangular plates, J. Appl. Mech. ASME 40 (1973) 298–299.
[30] S.P. Timoshenko, J.N. Goodier, Theory of Elasticity, 3rd ed., McGraw Hill, New York, 1970.
[31] S.P. Timoshenko, Theory of Plate and Shells, McGraw-Hill, New York, 1940.